Sensitivity Studies of Power Imbalance and Asymmetry for NIF Indirect Drive

O. S. Jones *S. M. Pollaine*

S. W. Haan *D. R. Speck*

J. T. Hunt *L. J. Suter*

Introduction

The time-averaged radiation asymmetry on a National Ignition Facility (NIF) capsule must be kept to a minimum to achieve high-yield implosions. The radiation asymmetry has an intrinsic component and a random component. Intrinsic asymmetry of the drive arises from a finite number of laser spots on the hohlraum, the presence of laser entrance holes, and coupling of Legendre modes between the cylindrical hohlraum and a spherical capsule. Random asymmetry arises from random variations in the power and pointing of each laser spot.

The emphasis of this article is on random asymmetry. The NIF requirements for power balance and pointing accuracy have already been established. The power balance requirement states that the rms "... deviation in the power delivered by the laser beams from the specified power shall be less than 8% of the specified power averaged over any 2-ns time interval." Similarly, the pointing specification allows for a 50-μm rms deviation in the centroids of the laser spots from their desired locations in the target plane. These specifications are based, in part, on the results of previous radiation viewfactor and radiation hydrodynamics calculations.[1]

Our work is a refinement of the earlier work and differs from it in two ways. First, the illumination geometry and laser configuration have changed substantially since the earlier work was done. The previous work was based on a design using 192 independent laser spots, whereas the NIF is now configured to have 48 quads, with each quad made of four beamlets. The spots from each beamlet in a quad overlap on the hohlraum wall, and the power to each beamlet in a quad is not completely independent because the same preamplifier module (PAM) feeds all beams in a quad. Second, rather than simply randomly varying the laser power to each spot, we have created a statistical model of the NIF laser and used it to predict power balance as a function of time for a given pulse shape.

Figure 1 shows laser power versus time for a single outer-cone beam for the NIF-baseline, 1.8-MJ, indirect-drive pulse. (For indirect drive, the beams are divided into inner and outer cones, and pulse shapes for each are slightly different.) We refer to the initial, low-intensity part of the pulse (roughly, the first 14 ns of the pulse) as the foot. We refer to the remainder of the pulse as the peak. Our overall approach to estimating flux asymmetry on the capsule for this pulse consisted

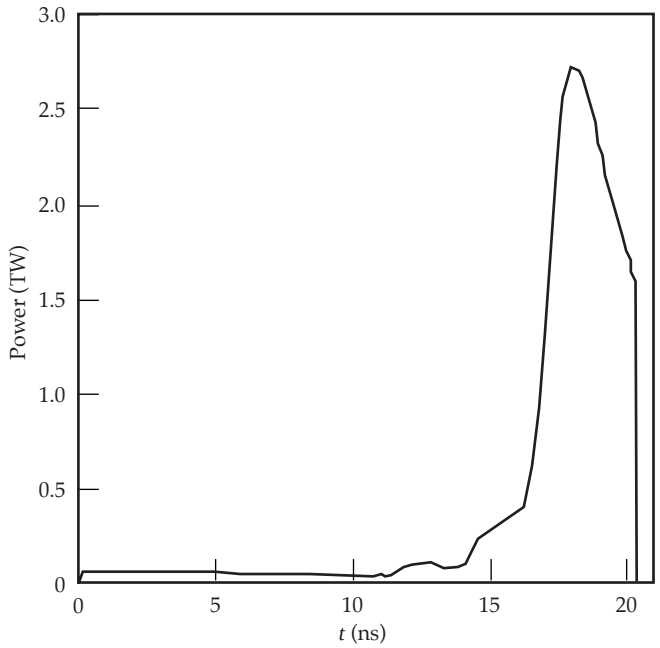

FIGURE 1. Laser power versus time for a single outer-cone beam for the NIF-baseline, 1.8-MJ, Haan indirect-drive pulse.
(50-00-1298-2545pb01)

of first estimating the random variations in laser power and pointing as a function of time. To do so, we developed a statistical model of the NIF laser system. Next, we used the radiation viewfactor code (Gertie, which is described in more detail later) to relate the random power and pointing distributions to flux asymmetry on the capsule at two times: the middle of the foot and the middle of the peak. Finally, we decomposed the flux asymmetry into Legendre modes and used linear growth factors from LASNEX capsule calculations to estimate the magnitude of each mode at ignition.

This article first describes the results of the statistical model of the NIF laser power balance. The calculation yields beam-to-beam and quad-to-quad power balance as a function of time. Next, we describe the radiation viewfactor calculations. These calculations yield the sensitivity of capsule flux asymmetry and spatial rms at ignition to the amount of power imbalance and pointing error. Finally, we provide our best estimate of capsule flux asymmetry during the foot and peak, from the power balance results, and use linear response coefficients to estimate the peak-to-valley variation in the hot-spot radius at ignition.

Laser Power Imbalance

The time-averaged (2-ns averaging time) deviation in power of a given beam, $P(t)$, from the desired power curve $P_0(t)$ is

$$\frac{\Delta P(t)}{P_0(t)} = \frac{1}{2}\int_{t-1}^{t+1} \frac{P(u)-P_0(u)}{P_0(u)}\, du \ , \qquad (1)$$

where u is a dummy variable of integration. The rms power imbalance is then

$$\sqrt{\frac{1}{N}\sum_{j=1}^{N}\left(\frac{\Delta P(t)}{P_0(t)}\right)_j} \ , \qquad (2)$$

where N is the total number of power-versus-time curves over which we average. For example, if we average over 10 shots and all 192 beams, then N is 1920. The NIF requirement is that the rms power imbalance must be less than 8%.

Power balance is a systemwide issue on the NIF. A certain level of random variations (also referred to as shot-to-shot variations or jitter) in power output of a given beam will occur, and this level will depend on the jitter levels of various laser subsystems. In addition to shot-to-shot variations, each of the 192 beams will, on average, yield a different output pulse if given identical input pulses. Such repeatable or systematic differences among beams must be minimized to meet the power balance requirement. In addition, the power measurement system must accurately measure the power history so that adjustments can be made to bring the output to the required balance.

We have developed a computer model of the NIF laser system to estimate the power balance. The model has been used to determine the allocation of random variations to subsystems, and to develop procedures for minimizing repeatable differences among beams.

NIF Power Balance Model

Two types of variations in laser performance lead to power imbalance: random (shot-to-shot) variations and systematic (repeatable) variations. Figure 2 identifies the sources of random and repeatable variations in beam power that are included in our model. The sources are the optical pulse generation (OPG) subsystem, the 1-μm laser, and the frequency-conversion and ultraviolet (UV) optics (0.35-μm) subsystem. Systematic differences are caused by differences in gain, transmission, beam area, and frequency conversion that repeat from shot to shot. Random variations are caused by shot-to-shot fluctuations in the OPG output (pulse injected to main laser), amplifier gain, pulse arrival time, and frequency conversion. In addition, a 4% rms random uncertainty arises from measurement of the power.

The laser-output pulse for a given injected pulse is predicted using the BTGAIN code.[2] BTGAIN models the propagation of an optical pulse through a laser chain consisting of a series of components having specified transmissions and gains. For the calculations in our study, the transmissions and gains represent average values over the beam cross-sectional area. Elements having gain (amplifier slabs) are modeled using Frantz–Nodvik theory,[3] which accounts for the gain depletion of an amplifying medium as an optical pulse travels through it.

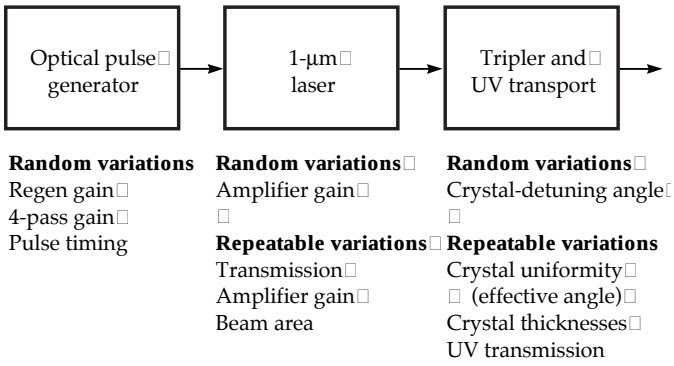

FIGURE 2. Schematic of the NIF laser showing sources of power balance included in the model. (50-00-1298-2546pb01)

Frequency conversion is calculated within BTGAIN from a table relating 1ω input intensity to 3ω output intensity. The conversion table is generated in a separate step by the THGFT02 code,[4] which calculates the frequency conversion for an arrangement of conversion crystals of given thicknesses and angles with respect to the beam axis (detuning angles). A decrease in frequency-conversion efficiency with imposed bandwidth is included.

The NIF model consists of 192 beams having repeatable differences in performance. That is, given identical input pulses, the beams produce different output pulses. The repeatable differences are modeled by assuming a random variation in optical properties (transmission, gain, frequency-conversion efficiency, and so forth) of the components that make up each beam. Table 1 shows the mean values and standard deviations of the amplifier gain coefficient and transmissions of optical components. The gains and transmissions are assumed to obey a Gaussian distribution. The mean values and standard deviations in Table 1 are consistent with the NIF optical specifications for the various components.

Each of the 192 beams has its own frequency-conversion curve (3ω versus 1ω intensity) that represents the repeatable performance of each converter. The baseline frequency converter has a doubler crystal thickness of 11.0 mm, a tripler crystal thickness of 9.0 mm, a doubler detuning angle of 240 μrad, a tripler detuning angle of 30 μrad, and 30 GHz of bandwidth. Systematic differences in frequency conversion are assumed to arise from beam-to-beam variations in average crystal thickness and from beam-to-beam variations in the effective detuning angle between the beam axis and the doubler crystal (the tripler crystal conversion is relatively insensitive to angle).

Figure 3 shows the power imbalance for beams with crystal thickness or doubler detuning angle different from that for the reference converter, compared to the same beam with the reference converter. We assume the doubler thickness varies uniformly from 11.0 to 11.2 mm, resulting in a 2% variation in frequency-conversion efficiency at the foot intensity, and less variation at higher intensity. Similarly, the tripler thickness varies from 9.0 to 9.2 mm, which results in a 3% variation in conversion efficiency at the foot intensity, and less at higher intensity.

Spatial nonuniformities in the crystals cause the local detuning angle to vary across a given crystal. The spatial variation in angles will differ for each crystal, so the overall (spatially integrated) conversion efficiency will vary systematically from beam to beam. We assumed that the distribution of conversion efficiencies among beams could be modeled by a Gaussian spread in the doubler detuning angle with a standard deviation of 28.6 μrad. The result is about a 3.5% rms deviation in frequency-conversion efficiency at the foot intensity, and less deviation at higher intensity. Because our assumption is highly conservative, actual systematic differences among crystals should be less than this value.

In addition to systematic differences among the 192 beams, the output of each beam will vary randomly from shot to shot about its average. Random variations in laser output depend on several factors,

TABLE 1. Mean and standard deviation (sigma) of component gains and transmissions.

Component	Mean value	Sigma
Amplifier gain coefficient	0.05/cm	0.00125/cm
Transmission coefficients		
Laser glass at Brewster's angle	0.9945	0.0015
Sol gel AR per surface	0.995	0.0015
KDP switch crystal	0.934	0.002
Polarizer transmission	0.97	0.005
Polarizer reflection	0.98	0.002
Multilayer dielctric mirror	0.99	0.0015
Doubling-crystal AR per surface	0.995	0.0015
Tripling-crystal AR per surface	0.995	0.0015
Focus lens	0.99	0.0015
Color-separation grating	0.977	0.005
Kinematic phase plate	0.97	0.003
Debris shield	0.98	0.003

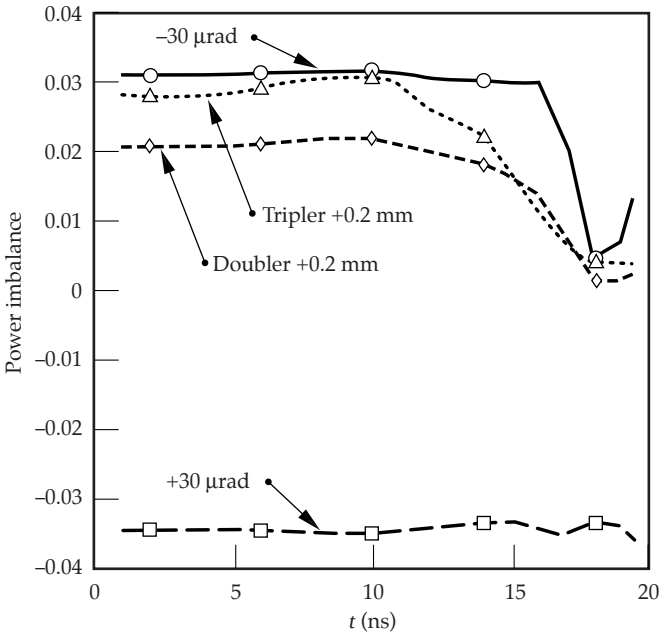

FIGURE 3. Power imbalance versus time for beams having different frequency-conversion crystal thicknesses or detuning angles than the reference beam. (50-00-1298-2547pb01)

some of which are correlated for beams in the same quad or bundle (a bundle is a pair of quads driven by a common set of capacitor banks). The fact that some variations are correlated among beams is important because the power imbalance will be greater than if the beams were completely independent.

Table 2 lists the sources of jitter in measured power, shows the allowable rms variation for each source (in some cases, values were established as a result of this study), and shows how the source is correlated among beams. For example, random variations in the injected pulse from the OPG are due to variations in gains of the regenerative and rod amplifiers that are part of each PAM. Because there is one PAM per quad, this source is correlated for beams within a quad. Pairs of quads (bundles) are driven by common capacitor banks, so the jitter in the main amplifier gains is correlated for the eight beams in a bundle. Jitter in the pulse-arrival time results in power imbalance only when the pulse shape is changing. For the Haan pulse, timing jitter contributes a maximum of 3.2% rms power imbalance during the period of steepest slope just before peak power. The allocated jitter in the doubler detuning angle (from jitter in the beam angle) results in 1.9% rms variation in frequency conversion at the foot intensity, and less at higher intensity.

Influence of Frequency Conversion and Gain Saturation on Power Balance

Frequency conversion and gain saturation have large effects on the time-dependence of power imbalance for shaped pulses. First, the intensity dependence of conversion efficiency amplifies the 1ω power imbalance, especially at low intensity. Second, gain saturation tends to reduce power imbalance, especially late in the pulse when gain saturation is greatest. Both factors tend to make the power imbalance the largest at the beginning, or foot, of the pulse when the intensity is lowest.

Figure 4 shows conversion efficiency as a function of 3ω intensity. At an intensity of 0.043 GW/cm^2, which corresponds to the foot of the Haan, 1.8-MJ, indirect-drive pulse, the frequency-conversion efficiency increases rapidly with increasing intensity. At the peak intensity of the Haan, 1.8-MJ pulse, the variation with intensity is much less.

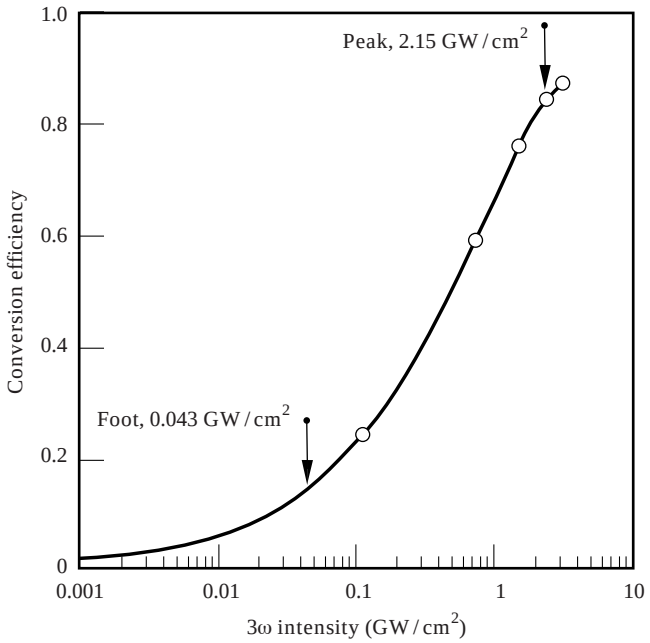

FIGURE 4. Frequency-conversion efficiency versus 3ω intensity. (50-00-1298-2548pb01)

In general, 3ω intensity out of the frequency converter is related to 1ω intensity into the converter by

$$I_{3\omega} \approx I_{1\omega}^{n} \quad , \tag{3}$$

where the exponent n varies between 3 at very low intensities and 1 at very high intensities. Taking the logarithmic derivative of this expression, we find that the change in intensities is related by

$$\frac{\Delta I_{3\omega}}{I_{3\omega}} = n \frac{\Delta I_{1\omega}}{I_{1\omega}} \quad . \tag{4}$$

Figure 5 shows the exponent n as a function of 3ω intensity. In the foot of the pulse, the 1ω power balance entering the frequency converter is amplified by a factor of 2.4. At the peak of the pulse, the amplification

TABLE 2. Subsystem allocations and correlations for sources of random power imblance.

Source	Allocation	Correlation
Injected power (from OPG)	3%	Beams in a quad (4)
Amplifier gain	2%	Beams in a bundle (8)
Frequency conversion	16 μrad	Uncorrelated
Pulse timing	30 ps	40% quad, 60% uncorrelated
Measurement	4%	Uncorrelated

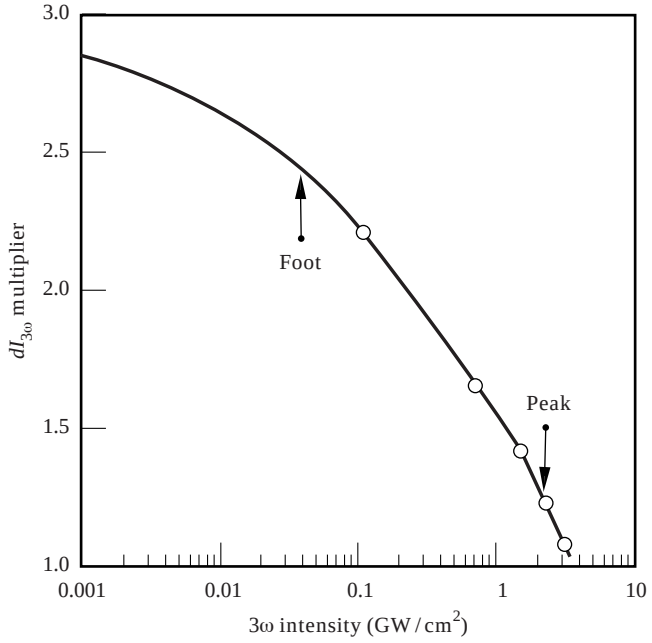

FIGURE 5. 1ω to 3ω power imbalance amplification factor versus 3ω intensity. (50-00-1298-2549pb01)

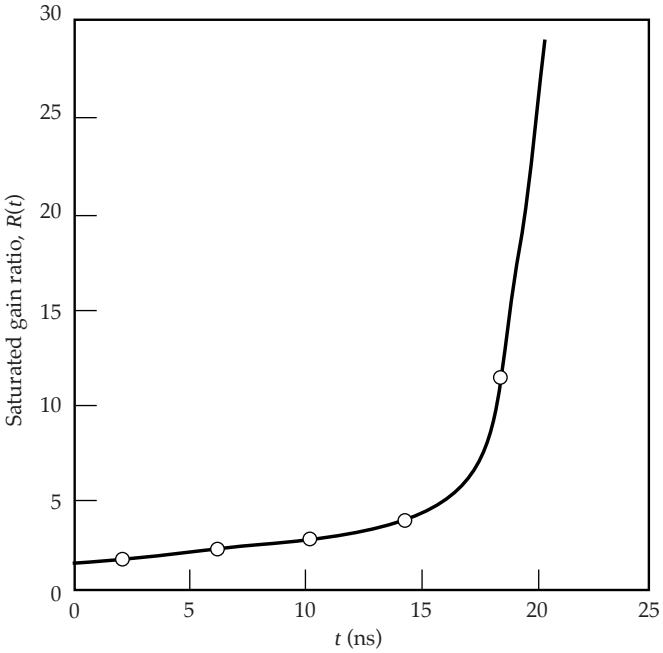

FIGURE 6. Saturated gain ratio versus time for the 1.8-MJ Haan pulse. (50-00-1298-2550pb01)

is only about 1.2.

As energy is extracted from amplifier slabs during a laser pulse, fewer excited atoms remain in the glass, and the gain is reduced. We call the ratio of small signal gain to actual gain the saturated gain ratio (or square pulse distortion). Figure 6 shows the saturated gain ratio as a function of time during the Haan pulse. The ratio increases from about 1.7 at the beginning of the pulse to more than 20 by the end. The reason the gain ratio is not 1 at $t = 0$ is that this is a multipass laser. During the final pass through the laser, even the foot of the pulse is passing through laser slabs that have already had significant energy extracted by previous passes of the entire pulse. The curve in Figure 6 is specific to the Haan pulse, but it is possible to write a more general expression for the gain ratio as a function of the amount of 1ω energy extracted from the laser. For a single-pass amplifier, there is a simple analytical expression; however, for the multistage, multipass NIF design, the expression is not so simple. Using BTGAIN, we obtained the following curve fit

$$R(E) = A \exp(BE), \tag{5}$$

where $E(t)$ is the ratio of amount of 1ω fluence (energy per area) extracted from the laser at a given time in a pulse to the saturation fluence (4.5 J/cm^2). The coefficients A and B depend on the total amount of normalized 1ω extracted fluence E_{tot}. The coefficients are

$$A = 0.79174 + 0.0093524\,(E_{tot}) + 0.0013361\,(E_{tot})^2\ , \tag{6}$$

and

$$B = 1.2078 - 0.55346(E_{tot}) + 0.56418\,(E_{tot})^2 - 0.22564(E_{tot})^3 + 0.035275(E_{tot})^4\ . \tag{7}$$

The expression is independent of pulse shape, and it applies for E_{tot} from 0.8 to 3.4. For the 1.8-MJ Haan pulse, E_{tot} is about 3.4.

If we know how the laser saturation and frequency-conversion exponent vary as a function of time for a given pulse, then we can estimate the random component of 1ω power imbalance as a function of time. Ignoring timing errors, the variation in 1ω power depends on the amount of variation in injected power (from the OPG) and the gain. Using a simplified analysis for a single-pass laser, and assuming that the logarithmic derivatives of the injected power and gain do not change significantly during the pulse, the 1ω power balance is related to these two sources by

$$\frac{\Delta P_{1\omega}(t)}{P_{1\omega}(t)} = \frac{1}{R(t)}\left(\frac{\Delta P_{inj}}{P_{inj}} + \frac{\Delta G_0}{G_0}\right)\ . \tag{8}$$

As energy is extracted from the laser, the gain ratio increases, and 1ω power imbalance decreases. To obtain the contribution of this part of the 1ω power

imbalance to 3ω power imbalance, we simply multiply the above expression by the frequency-conversion exponent. By adding this contribution in quadrature with estimates of the remaining contributions to power imbalance, we could estimate the power imbalance as a function of time. However, for highly saturated pulses, it is more accurate to extract the time-dependent 3ω power imbalance directly from BTGAIN calculations, which is what we have done in this work.

Minimizing Systematic Variations in Laser Power

By systematic variations in laser power, we mean that if the same pulse is repeatedly injected into a given laser beam, it will, on average, yield an output pulse that differs somewhat from the output pulse of the average beam. Systematic differences can arise from several factors, including differences in beam area, component transmissions, amplifier gains, and frequency conversion. Systematic variations in laser-power output must be made as small as possible for the system to meet the power balance requirement.

The simplest and most effective way to compensate for systematic differences is to increase the injected energy to consistently low beams and decrease injected energy to consistently high beams to minimize the systematic power imbalance at $t = 1$ ns, where the power imbalance is always highest for shaped, indirect-drive pulses. This approach works well because gain saturation and the intensity dependence of frequency conversion allow us to adjust the power in the foot of the pulse without changing the power imbalance in the peak very much.

Such a procedure requires setup shots in which all beams are given the same injected pulse, and the power in the foot of each pulse is measured and compared to the average value. The injected pulse is a nearly flat, 20-ns pulse that yields a flat output pulse at the same intensity as the foot of the Haan pulse. Because the pulse is flat, power can be inferred from an energy measurement, whose accuracy is better (2.8%) than that of the power measurement (4%). By averaging over four shots for each beam, accuracy is further improved to 1.4%. The injected energy to each beam is then adjusted to eliminate the systematic difference in power at $t = 1$ ns. The energy to each beam is adjusted by setting the PAM energy and adjusting the half-wave plates in the optics that split the beam from the PAM into four beams.

Although it is somewhat surprising, it appears that using a single input pulse shape (calculated by BTGAIN using average laser components) for all 48 PAMs is sufficient. That is, setting 48 different input pulse shapes to tune out systematic quad-to-quad differences results in only a marginal improvement in power balance. Figure 7 shows the results of a simulation in which we compared the performance of 192 lasers with randomly selected 1ω components and identical frequency converters. For each beam, we used BTGAIN to compute the input pulse shape that resulted in exactly the same output pulse for all the beams. The curve labeled "192 pulse shapes" shows that the rms power imbalance is zero when these input pulse shapes are used. Next, we averaged the input pulse shapes for each pair of beams to obtain 96 different pulse shapes. We averaged the input pulse shapes for each set of four beams to obtain 48 pulse shapes (one for each quad). We then compared the cases to that for a single input pulse shape. There is little difference in beam-to-beam power imbalance when comparing 1 pulse shape to 48 pulse shapes.

Figure 8 shows the systematic rms power imbalance

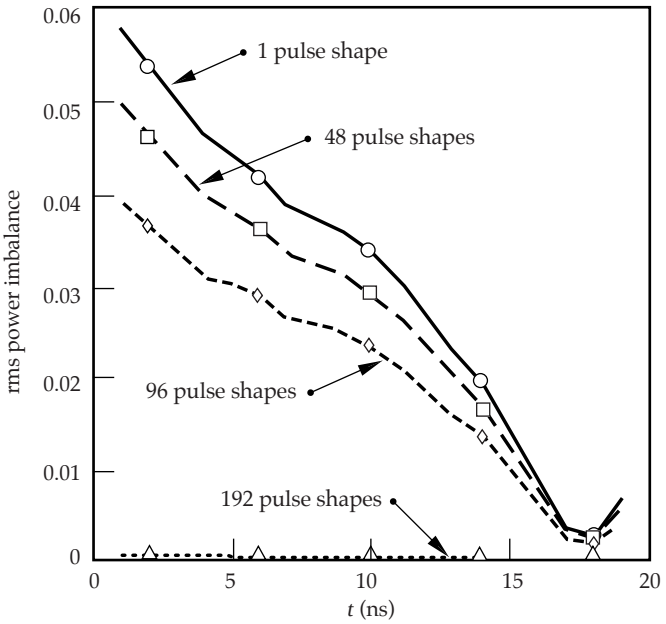

FIGURE 7. Sensitivity of systematic, beam-to-beam power imbalance to the number of independent pulse shapes. (50-00-1298-2551pb01)

(3ω) for the 192 beams of the power balance model with and without injection-energy correction. The upper curve is the systematic spread in power that arises from the differences in component performances when each beam is injected with the same energy. The uncorrected systematic power imbalance is clearly much too large to meet NIF requirements. The lower curve shows the rms power imbalance after adjusting injected energies to balance the power at $t = 1$ ns. It is

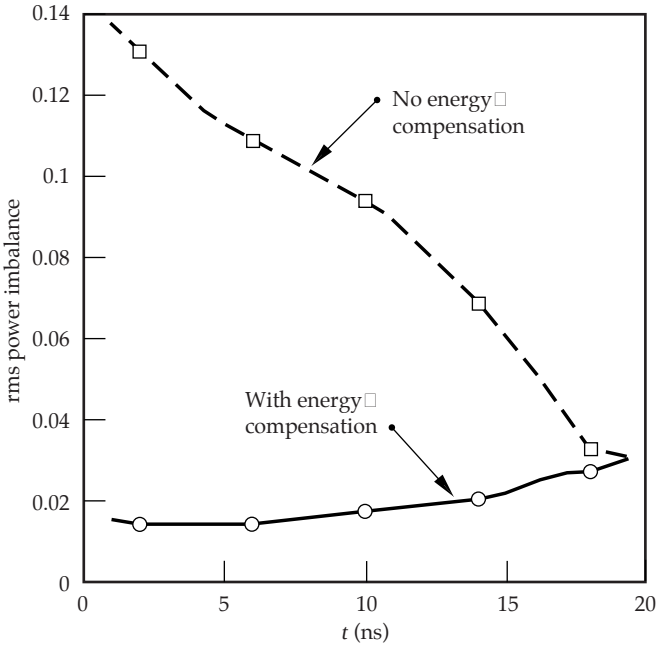

FIGURE 8. Systematic rms power imbalance as a function of time for the 1.8-MJ Haan pulse with and without injected-energy compensation. (50-00-1298-2552pb01)

approximately equal to the 1.4% measurement error at 1 ns, and rises to about 3% by the end of the pulse. In both cases, we used a single pulse shape.

Figure 9 shows the spread in injected energies of the 192 beams required to tune out systematic errors. The spread in energies is approximately Gaussian, with an 11% rms variation about the mean. The relatively large spread in energies is good, because it means the adjustment has some resolution. Figure 10 shows two histograms that compare the spread in 1ω power at t = 1 ns for the uncompensated case and the compensated case. Figure 11 shows the same kinds of plots, but for 3ω power at the target. Without compensation, the 1ω systematic rms power imbalance is 5.65%, which is then amplified by the frequency-conversion process to 13.8%.

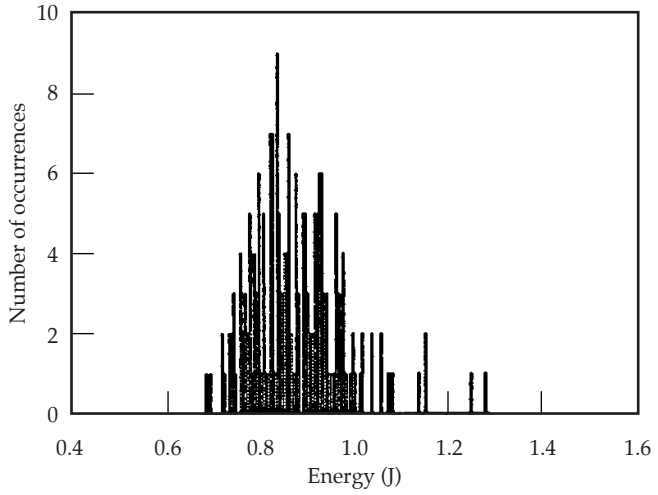

FIGURE 9. Histogram of the spread in injected energies required to tune out the t = 1 ns power imbalance. (50-00-1298-2553pb01)

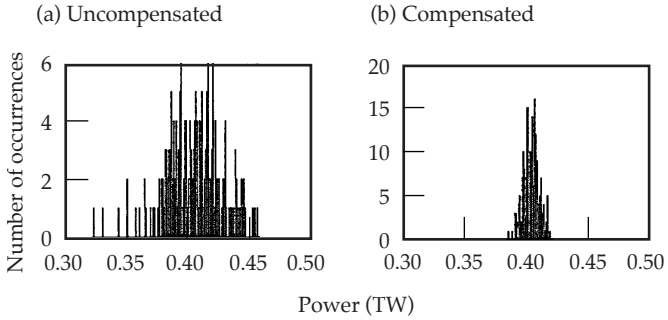

FIGURE 10. Histograms comparing the spread in 1ω power at t = 1 ns for the (a) uncompensated and (b) compensated cases. (50-00-1298-2554pb01)

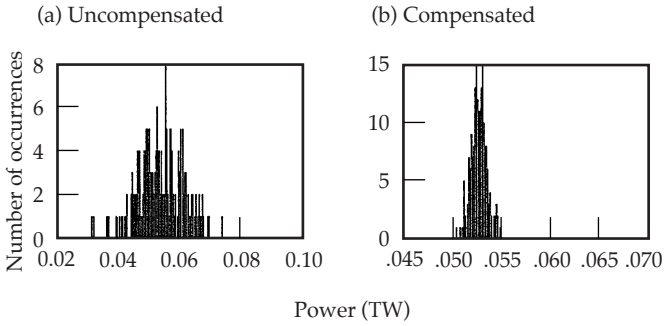

FIGURE 11. Histograms comparing the spread in 3ω power at t = 1 ns for the (a) uncompensated and (b) compensated cases. (50-00-1298-2555pb01)

Estimate of Overall Laser Power Imbalance

We included all known sources of random and systematic errors to obtain an estimate of the overall power imbalance. Such an estimate can be used as a basis for the flowdown of requirements to the subsystems and to confirm that our strategy for minimizing systematic power balance errors will result in a total error that meets the NIF power balance requirement. We averaged over 192 beams and 10 shots (1920 power-versus-time curves) to obtain the rms values for these calculations.

Figure 12 shows beam-to-beam, quad-to-quad, and intraquad rms power imbalances versus time. The beam-to-beam imbalance for a single calculation can be obtained from Eqs. (1) and (2), with N = 192. We then take the rms average over the number of runs to obtain the final result. The quad-to-quad imbalance is

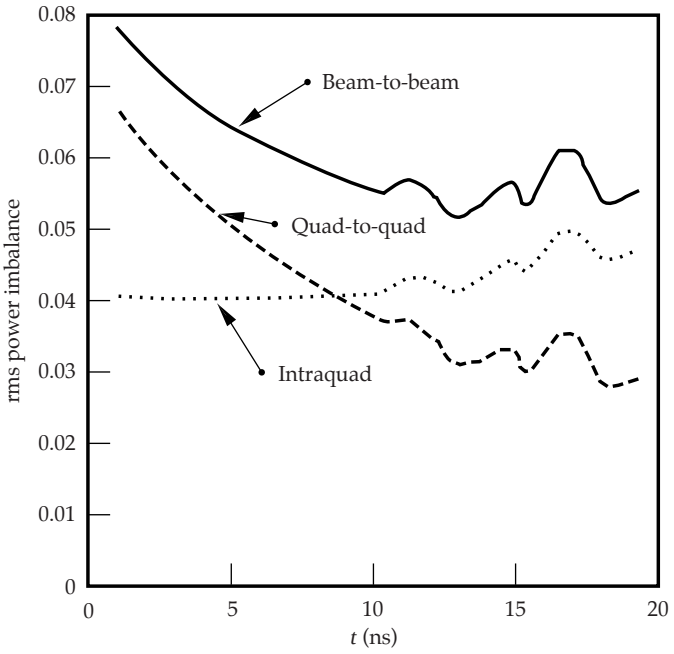

FIGURE 12. Total rms power imbalance versus time for the 1.8-MJ Haan pulse. (50-00-1298-2556pb01)

obtained by averaging over the four beams in each quad to obtain the power in each quad, taking the rms average over the 48 quads, and then taking the rms average over the number of runs. The intraquad imbalance is a measure of the imbalance for beams in the same quad. It is the square root of the difference between the square of the beam-to-beam imbalance and the square of the quad-to-quad imbalance. The rms beam-to-beam power imbalance is 7.8% at $t = 1$ ns, and decreases to about 6% by the end of the pulse. The bumps in the curve appearing late in the pulse are due to timing jitter during pulse-shape changes. The value we obtained is less than the NIF 8% limit for the entire pulse. To meet the overall NIF power balance requirement, we reduced the allowable random variation in amplifier gain from its original allocation of 3% to 2%.

If the beams were completely independent, then the quad-to-quad imbalance would be exactly half the beam-to-beam imbalance because the power in each quad would be the average of four independent quantities. Early in the pulse, power imbalance is dominated by the OPG and amplifier jitter, which are correlated for beams within a quad, so the quad-to-quad imbalance is much more than half of the beam-to-beam imbalance. By the end of the pulse, these sources of imbalance make a relatively small contribution to the total, and the beams are largely uncorrelated. This is an important result because, as shown next, capsule flux asymmetry depends most directly on quad-to-quad power imbalance.

Calculations of Radiation Asymmetry on a NIF Capsule

Here, we describe our calculations of the effects of random variations in laser power and pointing on radiation flux symmetry at the target. We estimated the sensitivity of capsule flux asymmetry to various amounts of power imbalance and pointing errors, and then used our results from the detailed laser model, described above, to estimate the expected capsule flux asymmetry during the foot and peak of a shaped, indirect-drive pulse.

Calculating the Random Component of Radiation Flux on a Capsule

We used the radiation viewfactor code, Gertie,[5] to estimate the flux on a capsule. The geometry of the hohlraum and capsule are the primary inputs to the code. The surfaces of each are divided into a discrete number of area elements A_i. Each element has an albedo α_i, which is the ratio of emitted radiation over absorbed radiation, averaged over all frequencies and angles. In addition, surface elements on the hohlraum wall that correspond to laser hot spots are given a source power P_i. Radiation power leaving the ith element y_i, and radiation power arriving at that element x_i, are related to each other by

$$y_i = \alpha_i x_i + P_i \tag{9a}$$

and

$$x_i = \sum_j f_{ij} y_j \ , \tag{9b}$$

where f_{ij} is the geometric viewfactor matrix constructed by Gertie. Thus, once the geometry, albedos, and radiation sources are defined, the matrix equations can be solved to obtain the radiation flux incident on the capsule (and on all other surfaces as well). The viewfactor analysis has two principal limitations. Sources and albedos are not frequency-dependent, and there is no absorption and emission of radiation by the plasma inside the hohlraum (i.e., vacuum transfer is assumed between the walls and capsule). However, the technique does provide an estimate of the 3D variation of flux on the capsule.

Viewfactor calculations were done for the point-design target[6] (PT design), which is shown in Figure 13. This target has a 0.111-cm radius and uses a Br-doped plastic ablator. It is driven by a 1.3-MJ, 17-ns pulse, shown in Figure 14. This pulse is similar to the 1.8-MJ, NIF-baseline pulse shown earlier; however, the foot is about 3-ns shorter, and the peak power and energy are

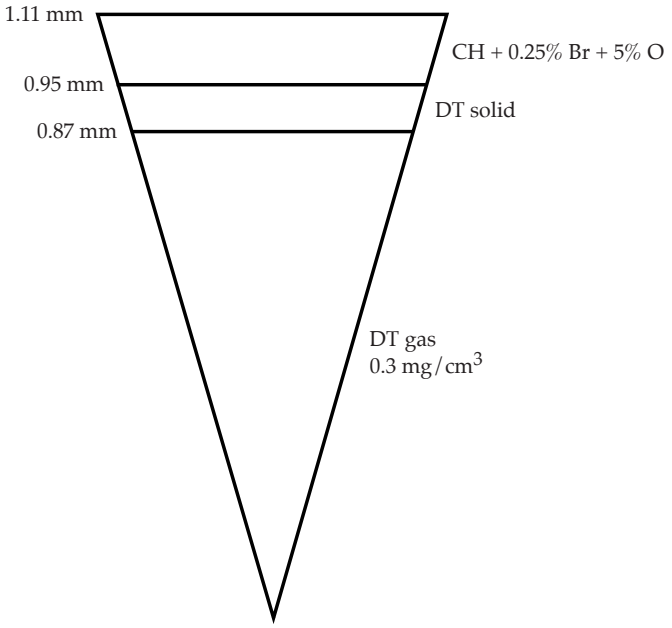

FIGURE 13. The PT design features a Br-doped plastic ablator and has an initial radius of 0.111 cm. (50-00-1298-2557pb01)

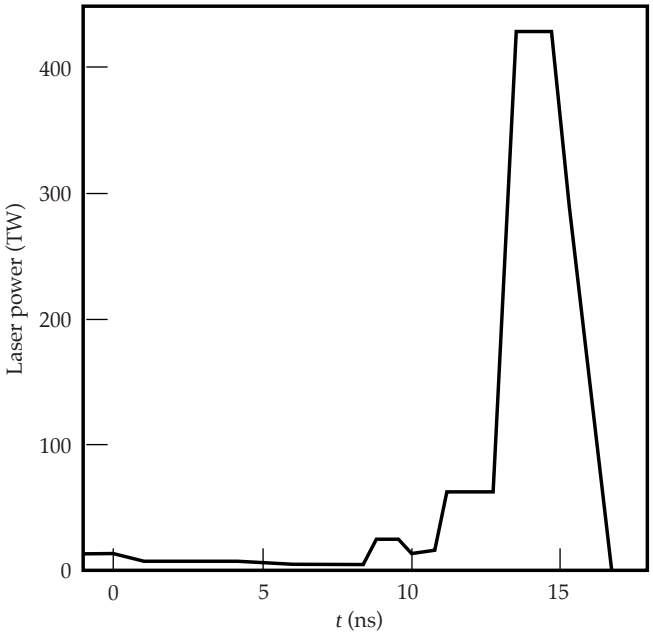

FIGURE 14. The PT is driven by a 17-ns, 1.3-MJ, shaped pulse. (50-00-1298-2558pb01)

less. From radiation-hydrodynamics calculations of the PT design using LASNEX,[7,8] we inferred the time dependence of the capsule and hohlraum albedos, the capsule ablation surface radius, and the hohlraum emission radius (which moves in as gold blows off the wall).

The albedo of the gold wall is greater than that of the plastic ablator, and both increase as radiation temperature rises during the pulse. As the albedo increases, a smaller fraction of total radiation emanates from the laser hot spots, and the radiation is spatially smoothed. In addition, as the hohlraum emission radius and capsule ablation surface radius both decrease with time, the viewfactor matrix that maps the hohlraum radiation onto the capsule also changes. Late in the pulse, as the capsule ablation surface radius decreases rapidly, each point on the capsule sees a larger fraction of the hohlraum wall; therefore, higher wave number components of the radiation asymmetry on the hohlraum are smoothed at the capsule.

In principle, we could divide the pulse into a few time steps and do a viewfactor calculation at each time to obtain the time-dependent flux on the capsule. However, we found it more practical to divide the pulse into two parts. We defined the foot to be the first 11 ns, and the peak to be the remainder of the pulse. We then did the viewfactor analysis midway through the foot and midway through the peak, using average values for the albedos and dimensions shown in Table 3. We subdivided the capsule and hohlraum surfaces into 3,840 subpanels, with 32 panels per 360° of azimuthal angle.

TABLE 3. Geometric parameters and albedos used in the viewfactor calculations of the foot (t = 0 to 11 ns) and peak (t = 11 to 17 ns).

Parameter	Foot	Peak
Hohlraum albedo	0.65	0.86
Capsule albedo	0.35	0.63
Hohlraum radius	0.27 cm	0.234 cm
Hohlraum length	1.0 cm	0.95 cm
LEH radius	0.135 cm	0.117 cm
Capsule radius	0.111 cm	0.085 cm

Estimating Capsule Perturbation Resulting from Radiation Asymmetry

If we denote the radiation on a capsule as F, then rms flux asymmetry at the capsule is

$$cap_{\mathrm{rms}} = \sqrt{\frac{1}{4\pi}\int\left(\frac{F-F_0}{F_0}\right)^2 d\Omega} \quad . \tag{10}$$

The flux can be expanded, in terms of associated Legendre polynomials, as

$$F(\theta,\phi) = \sum_{l=0} b_{l0} P_l^0 + \sum_{l=1} \sum_{m=l}^{l} 2 b_{lm} P_l^m \times \cos m\phi$$

$$- \sum_{l=1} \sum_{m=-l}^{l} 2 b_{lm} P_l^m \sin m\phi \quad . \tag{11}$$

This form of the expansion is the same as that computed by the Gertie viewfactor code. By substituting Eq. (11) into Eq. (10) and including the appropriate normalization factors, we can express the rms flux asymmetry as the root of the sum of squares of contributions from each mode. That is, the capsule asymmetry is

$$cap_{\mathrm{rms}} = \sqrt{\sum_{l=1} \sum_{m=-l}^{l} \left(a_{lm}\right)^2} \ , \tag{12}$$

where

$$cap_{\mathrm{rms}} = \sqrt{\sum_{l=1} \sum_{m=-l}^{l} \left(a_{lm}\right)} \tag{13}$$

and

$$a_{lm} = \sqrt{\frac{2}{2l+1} \frac{\left(l-|m|\right)}{\left(l+|m|\right)} \left(\frac{b_{lm}}{b_{00}}\right)^2} \quad . \tag{14}$$

For each l mode, we can sum the squares of the rms contributions for all m to obtain the rms for an equivalent 2D mode, which we denote as a_l.

Now that we have extracted the mode structure (rms per mode) of the equivalent 2D flux asymmetry from the viewfactor calculation, we can use LASNEX to calculate the spatial perturbation in the capsule radius at ignition due to each mode. As long as radiation-induced perturbations on the capsule remain linear, we can use the principle of superposition to equate the calculated 2D rms flux asymmetry at ignition to the rms flux asymmetry at ignition that results from linear growth of the original 3D spectrum of modes from the viewfactor calculation.

The linear response coefficients that relate a flux perturbation to spatial perturbation on the capsule for each mode were calculated in LASNEX by applying a frequency-dependent source to the capsule that had a small perturbation in each mode applied during the foot (0 to 11 ns) or peak (11 to 17 ns) of the pulse. These coefficients yield the capsule rms spatial asymmetry for the case where the 3D capsule flux asymmetry calculated at the midpoint of the foot or peak is present and unchanging for the entire foot or peak. This is a simplification of the actual situation, where the magnitude and mode structure of the capsule flux asymmetry change during the foot and peak.

NIF Illumination Geometry

Figure 15 shows the NIF indirect-drive geometry. Laser rays are shown from their focal points to the point at which they hit the hohlraum walls. Two cones, an outer and an inner cone, illuminate each side of the hohlraum. The outer cone is made of beams having angles of 44.5° and 50° with respect to the z (cylindrical) axis. The inner cone beams have angles of 23.5° and 30°. Two-thirds of the laser energy is directed to the outer cones, and one-third to the inner cones. Figure 15 also shows the target geometry that we assumed for this study. The hohlraum length is 1.0 cm, the hohlraum radius is 0.27 cm, laser entrance holes have a radius of 0.135 cm, and the initial capsule radius is 0.111 cm.

Spots from the four beams in a quad partially overlap on the hohlraum wall, forming one larger spot, as shown in Figure 16. Differences in power among the four beams in a quad cause a shift in the spot centroid and are equivalent to a pointing error in the quad spot. The distance from the centroid of the quad spot to centroids of each of the individual beam spots, r_j, is about 230 μm. The offset of the centroid of the quad spot, r_c, is related to beam power by

$$r_{\mathrm{c}} = \sum_{j=1}^{4} \frac{r_j P_j}{P_{\mathrm{quad}}} \ , \tag{15}$$

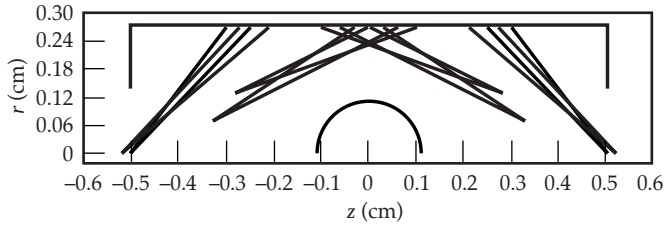

FIGURE 15. Side view of the hohlraum showing placement of inner and outer cones. (50-00-1298-2559pb01)

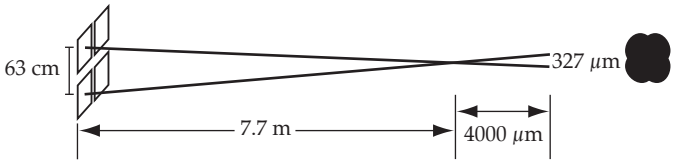

FIGURE 16. Four beams within a quad form a single, overlapped spot on the hohlraum. (50-00-1298-2560pb01)

where P_j is the power from the jth beam, and P_{quad} is the total quad power. Using Eq. (15), we can calculate that the 4% to 5% intraquad power imbalance, which was calculated previously in Figure 12, results in a 5- to 6-μm rms error in quad spot position.

Sensitivity of Ignition Capsule to Random Flux Asymmetry

Figure 17 shows the sensitivity of total rms capsule flux to the amount of quad-to-quad power imbalance using the viewfactors midway through the foot and peak of the pulse. These results were obtained by averaging over 10 sets of random power distributions that were generated using the statistical model of the NIF laser, discussed previously. We assumed that the viewfactor calculations done for a 17-ns pulse could be applied to the 20.4-ns Haan pulse. For the foot, we used BTGAIN results at $t = 7$ ns (midway through the 14-ns foot). For the peak, we used BTGAIN results at $t = 17$ ns (approximately midway through the peak). Figure 17 shows that, compared to the peak, the larger ratio of capsule radius to hohlraum radius for the foot, and the lower albedos in the foot, result in a larger amount of flux asymmetry. The average quad power imbalance during the foot of the Haan pulse is approximately 4%, and it is about 3% during the peak (see these two points as plotted in Figure 17). Thus, the resulting rms flux asymmetry due to power imbalance will be about 0.6% during the foot, and 0.2% during the peak. Note that rms flux asymmetry is plotted here as a function of the quad-to-quad imbalance, rather than beam-to-beam imbalance. As shown below, quad-to-quad imbalance can be generally related to asymmetry on the capsule, whereas beam-to-beam imbalance cannot.

The other contributor to random flux asymmetry is pointing errors. Figure 18 shows rms flux asymmetry on the capsule as a function of rms quad pointing error. The results were obtained by averaging over 50 random pointing configurations. By quad pointing error, we mean the deviation in the location of the quad centroid. The NIF specification for allowable beam-to-beam pointing errors is 50 μm rms. It is likely that there will be sources of pointing error that are common to beams within a quad; however, the breakdown between correlated and uncorrelated pointing errors has not been determined at this time.[9] If we assume that pointing errors are uncorrelated, then a 50-μm, beam-to-beam error corresponds to a 25-μm, quad-to-quad error, which leads to capsule flux asymmetry of about 0.4% during the foot, and less than 0.2% during the peak. Figures 17 and 18 are plotted on the same scale, and a comparison between them shows that power imbalance will generally have a larger effect on capsule flux asymmetry than will the pointing errors.

Recall from Eq. (12) that capsule flux rms asymmetry can be expressed as the root of the sum of squares of contributions from each associated Legendre polynomial. The square of the rms is called the variance. Thus, the variance per mode is a_{lm}^2, where a_{lm} is given by Eqs. (13) or (14). The variance per l mode, which is what we need to apply the 2D linear response coefficients calculated from LASNEX, is

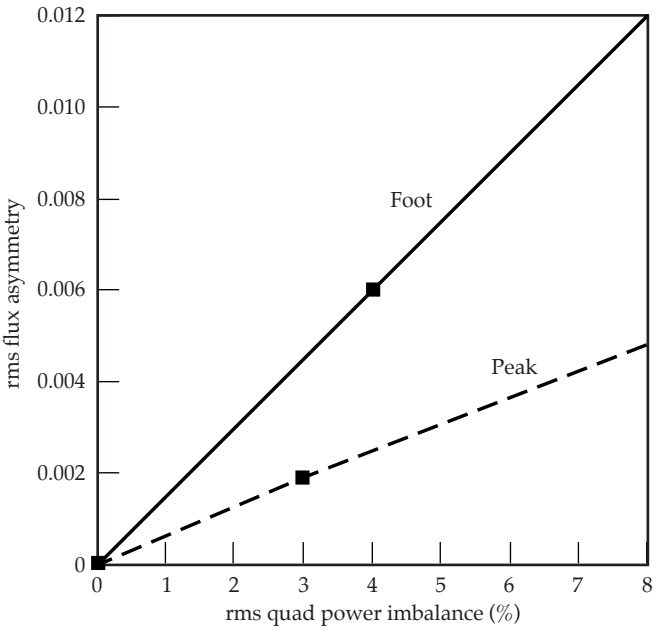

FIGURE 17. The rms capsule flux asymmetry as a function of amount of quad-to-quad power imbalance. (50-00-1298-2561pb01)

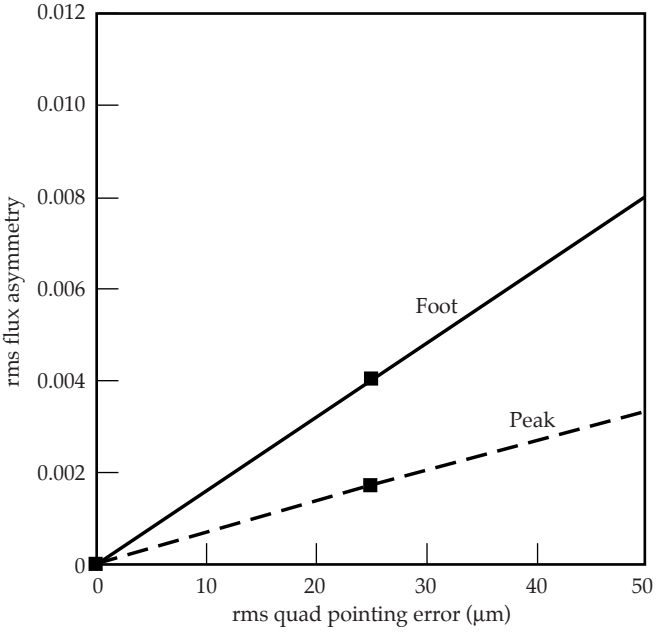

FIGURE 18. The rms capsule flux asymmetry as a function of quad-to-quad pointing errors. (50-00-1298-2562pb01)

$$a_l^2 = \sum_{m=-l}^{m=+l} a_{lm}^2 \quad . \tag{16}$$

The ratio of a_l^2 to total variance of capsule flux is plotted in Figure 19 as a function of l-mode number for power imbalance. For both the foot and peak, the largest contribution is from P_1, and there is little contribution from modes larger than $l = 4$. Figure 20 shows the modal decomposition for pointing errors. Similar to the power imbalance, the contribution to variance falls off rapidly with increasing mode number. However, the dominant mode is P_2, and there is a larger relative contribution from higher modes.

From the modal decomposition of flux asymmetry, we can find each mode's contribution to the capsule spatial asymmetry at ignition using the linear response coefficients obtained from LASNEX capsule calculations. The capsule spatial rms is given by

$$\left(\text{spatial}\right)_{\text{rms}} = \sqrt{\sum_{l=1}\left[a_l\left(\text{lrc}\right)_l\right]^2} \quad , \tag{17}$$

where $(\text{lrc})_l$ is the linear response coefficient relating capsule flux rms due to the lth mode to the spatial rms at ignition due to that mode. We multiply the spatial rms by 2 times the square root of 2 to convert the rms to the maximum difference in peak-to-valley (ptv) of the spatial variation. This parameter is plotted in Figure 21 as a function of percent rms quad power imbalance. Such a plot shows that the peak is slightly more sensitive to power imbalance than the foot, even though the capsule flux asymmetry is less for the peak. The shaded portion of the plot (6-μm ptv perturbation or less) represents the level of capsule perturbations arising from random asymmetry that is definitely

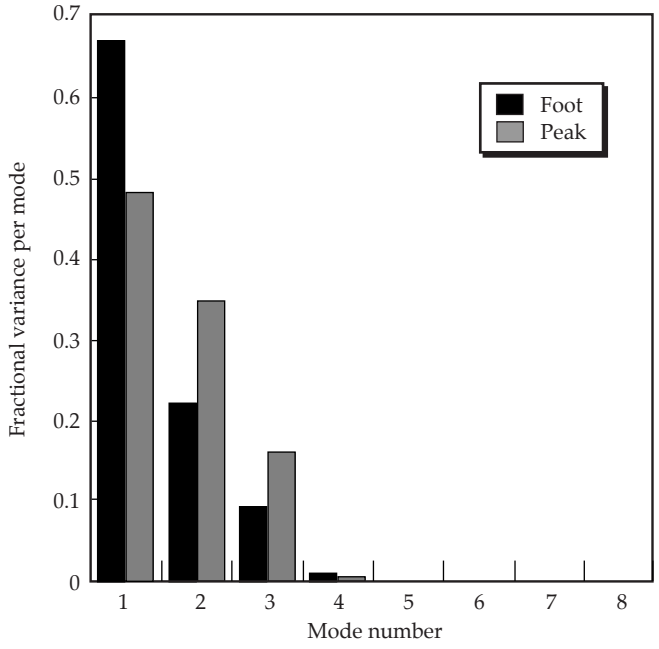

FIGURE 19. Fractional contribution of each Legendre mode to total variance of the capsule flux due to power imbalance.
(50-00-1298-2563pb01)

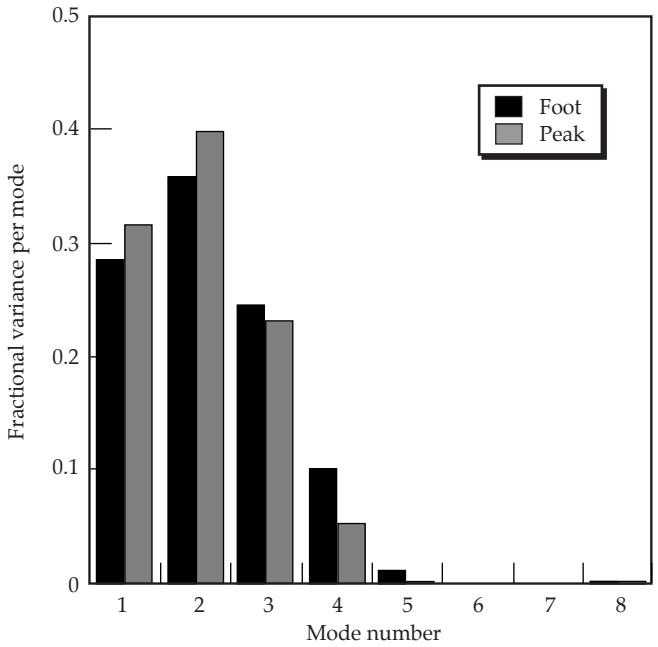

FIGURE 20. Fractional contribution of each Legendre mode to total variance of the capsule flux due to beam pointing errors.
(50-00-1298-2564pb01)

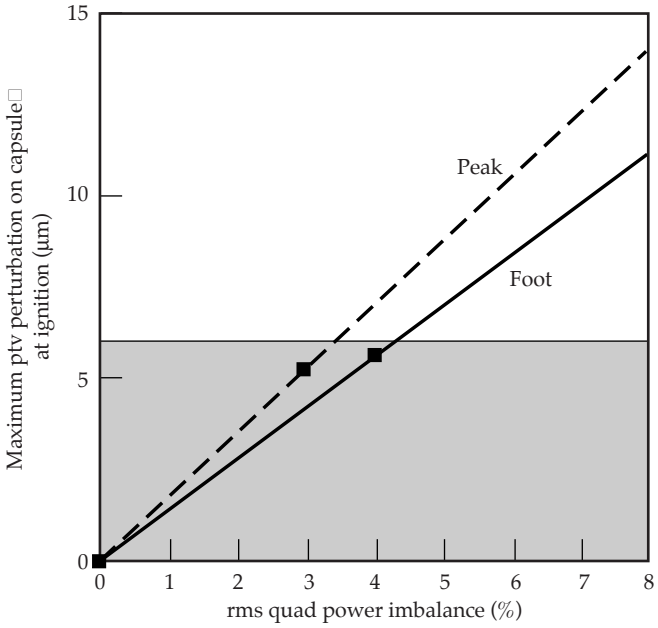

FIGURE 21. Maximum peak-to-valley perturbation in hot-spot radius at ignition as a function of percent rms quad power imbalance.
(50-00-1298-2565pb01)

safe.[10] Thus, the time-averaged quad power imbalance must remain well below 8% to keep the resulting spatial perturbations in the safe regime. At the power imbalance levels extracted from BTGAIN calculations (see data points), power imbalance only during the foot results in a 5.6-μm ptv perturbation, whereas power imbalance only during the peak results in a 5.2-μm ptv perturbation.

Figure 22 is a similar plot, but for pointing errors. It shows that if the pointing errors are uncorrelated, resulting in 25-μm rms quad-to-quad pointing error, then pointing errors make a slightly smaller contribution to the total capsule spatial perturbation at ignition (5.1 versus 4.3-μm ptv for the foot versus peak, respectively).

Figure 23 shows the fractional contribution of each mode to total variance (the square of the rms) of spatial asymmetry on the capsule. For the foot, P_1 and P_2 are the largest contributors, whereas for the peak, P_1 is by far the largest. In fact, it is primarily the much larger linear response factor for P_1 in the peak, compared with that of the foot, that makes the overall capsule rms larger for the peak, despite the fact that rms flux asymmetry is less for the peak due to hohlraum smoothing. Figure 24 is a similar plot for pointing errors. Pointing errors during the foot give rise mainly to modes P_2 through P_4 on the capsule surface at ignition, whereas pointing errors during the peak contribute mostly to P_1 on the capsule. The combined effects of power imbalance predicted by the BTGAIN model and 25-μm rms quad pointing errors result in a capsule spatial perturbation of 7.5-μm ptv for asymmetry imposed during the foot only, and 6.7-μm ptv for asymmetry imposed during the peak only.

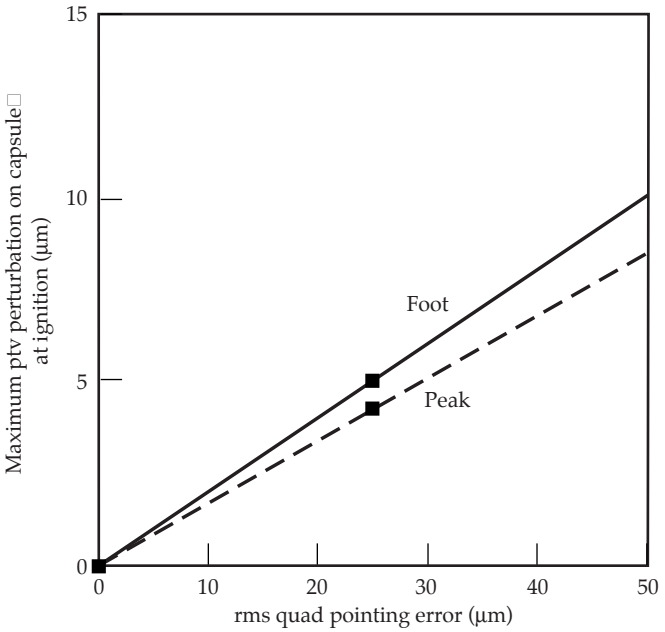

FIGURE 22. Maximum peak-to-valley perturbation in hot-spot radius at ignition as a function of percent rms quad pointing error. (50-00-1298-2566pb01)

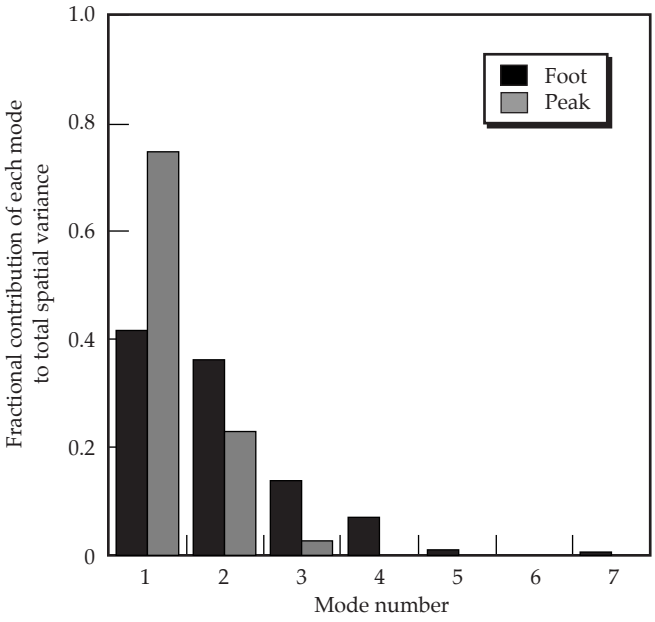

FIGURE 23. Fractional contribution of each Legendre mode to total variance of the hot-spot radius at ignition due to quad power imbalance. (50-00-1298-2567pb01)

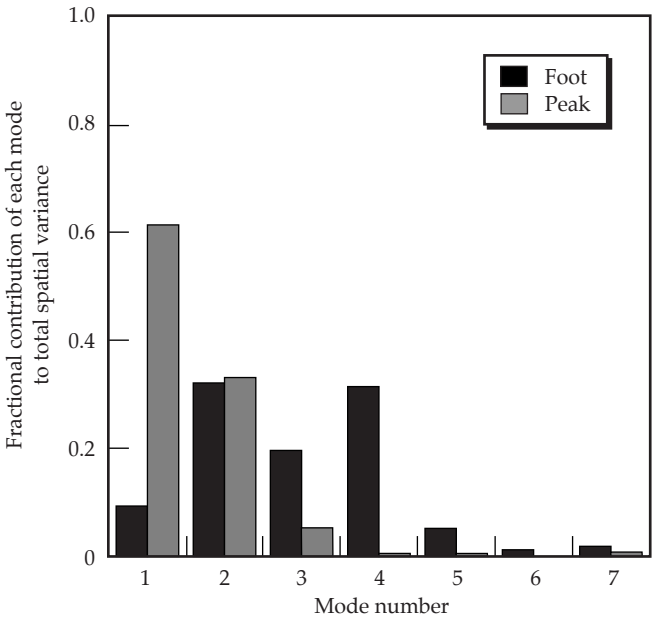

FIGURE 24. Fractional contribution of each Legendre mode to total variance of the hot-spot radius at ignition due to quad pointing errors. (50-00-1298-2568pb01)

Effect of Correlations on Power Balance

The powers to each of the 192 spots are not statistically independent. As discussed in the previous section, beams in a quad are driven by a common PAM, so the portion of the power imbalance arising from

jitter in the PAMs will be correlated for beams in the same quad. There is also a correlation between pairs of quads whose amplifiers are driven by common capacitor banks (such pairs of quads are called bundles), so jitter in amplifier gain will be correlated between bundles. Figure 25 is a schematic drawing of the overlapped quad spots on one-quarter of an unrolled hohlraum cylinder. The shading and numbers on the spots indicate which quads are driven by common capacitor banks. Correlated spots are separated from each other spatially in a pseudo-random pattern. The pattern repeats itself in the next quadrant. For the two remaining quadrants ($\pi < \phi < 2\pi$) the relation between bundles 5 and 6 is reversed.

The idea behind bundle mapping is to ensure that neighboring quads are not correlated; if they were, statistically they would behave like a single spot. This would increase the power imbalance due to the amplifier gain jitter by reducing the number of independent spots from 48 to 24.

To assess possible effects of correlations between beams on the power imbalance, we computed the power imbalance for three extreme cases:

Case 1. 192 independent beams.
Case 2. 48 independent quads, with the 4 beams within each quad correlated.
Case 3. 24 independent bundles, with the 8 beams within each bundle correlated.

The calculations were all done for the foot of the pulse. Figure 26 shows that the rms capsule flux asymmetry is about the same for a given amount of quad-to-quad power imbalance, regardless of how the power is correlated among the beams. This result indicates that quads in the same bundle are mapped to the hohlraum in a way that does not degrade capsule symmetry, even if all of the power imbalance were correlated for beams in the same bundle. Figure 27 shows the contribution of each mode to total spatial variance on the capsule at ignition. The modal structure is also fairly similar for the three cases. This result implies that the most important parameter needed to estimate capsule asymmetry due to power imbalance is an accurate estimate of quad-to-quad power imbalance. Knowing the fraction of quad-to-quad imbalance from beam-, quad-, and bundle-driven power imbalance is less important.

Summary

We have developed a model to analyze power balance for the NIF. Our model includes the effects of laser gain saturation and frequency-conversion intensity dependence. Statistical variation in component performance was included to account for systematic and random variations in the power output of each beam. We found that the effects of gain saturation, which tends to reduce power imbalance late in the pulse, and the strong intensity dependence of frequency conversion at low intensity early in the pulse, combine to make the power imbalance largest at the beginning of shaped, indirect-drive pulses. We then used the model to determine the allocation of random variations to subsystems and to develop procedures for minimizing repeatable differences among beams. The results of our power balance analysis indicate that we can meet the NIF 8% rms power balance requirement for a 1.8-MJ, indirect-drive pulse. To minimize

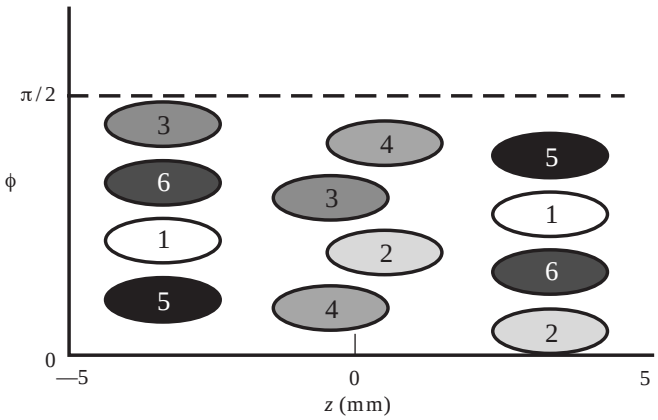

FIGURE 25. One-quarter of a hohlraum cylinder unrolled to show the approximate arrangement of overlapped quad spots on the hohlraum and the relative locations of quads sharing capacitor banks. (50-00-1298-2569pb01)

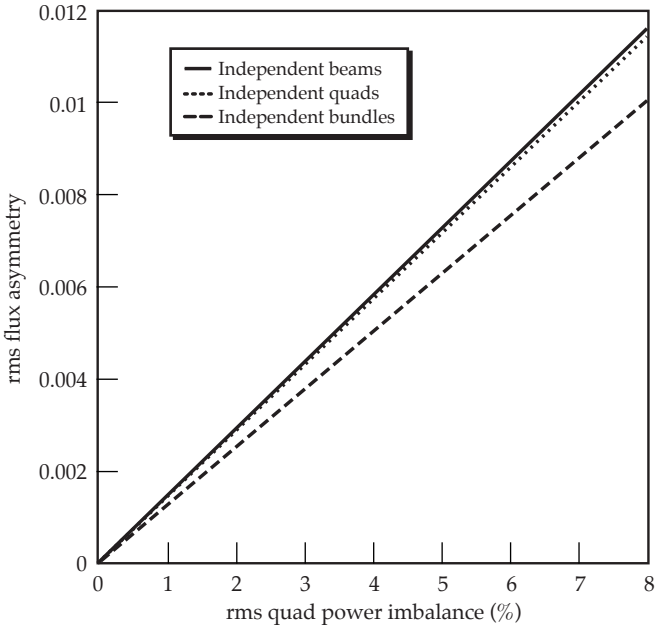

FIGURE 26. The rms capsule flux asymmetry in the foot as a function of rms quad power imbalance for 192 independent (uncorrelated) beams, 48 independent quads with all 4 beams in each quad correlated, and 24 independent bundles with all 8 beams in each bundle correlated. (50-00-1298-2570pb01)

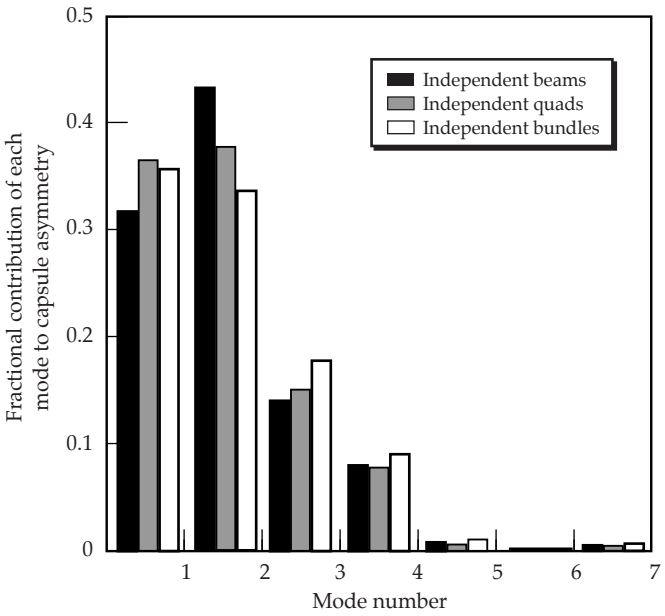

FIGURE 27. Fractional contribution of each Legendre mode to total variance of the hot-spot radius at ignition for power imbalance in the foot due to 192 independent beams, 48 independent quads with all 4 beams in each quad correlated, and 24 independent bundles with all 8 beams in each bundle correlated. (50-00-1298-2571pb01)

the systematic imbalance, we use a single-input pulse shape, but adjust the energy to each beam to minimize the repeatable power imbalance at $t = 1$ ns.

We also performed a radiation viewfactor analysis to determine the effect of various levels of random flux asymmetry on ignition capsule performance. The capsule rms flux asymmetry is larger—for a given level of imposed power imbalance or pointing errors—during the foot of the pulse than during the peak. The reason is that lower albedos and larger capsule-radius-to-hohlraum-radius ratio lead to less smoothing of the Legendre modes onto the capsule. However, the capsule is more sensitive to the P_1 mode during the peak. Thus, the resulting spatial perturbation on the capsule at ignition is about the same for radiation asymmetry imposed during the foot or peak. Power imbalances contribute slightly more to the total capsule perturbation at ignition than do pointing errors.

The fraction of power imbalance that is correlated for beams within the same quad is very important, because flux asymmetry on the capsule is twice as large for fully correlated beams than for fully uncorrelated beams. Our NIF laser modeling indicates that power imbalance is highly correlated early in the pulse when the power imbalance is dominated by OPG and amplifier jitter. By the end of the pulse, the largest sources of power imbalance (random variations in timing and frequency conversion, and all systematic variations) are mostly uncorrelated, which reduces the effect on the capsule. The fraction of power imbalance that is correlated between quads whose amplifiers are driven by common capacitor banks was found to be a minor effect.

Integrated viewfactor simulations that assumed a level of 50-μm rms uncorrelated pointing errors and a level of power imbalance extracted directly from the statistical NIF laser model indicate maximum peak-to-valley perturbations on the hot-spot radius at ignition of 7.5 μm due to random flux asymmetry applied only during the foot of the pulse, and 6.7 μm due to random flux asymmetry applied only during the peak of the pulse. These values are close to the maximum amount of capsule perturbation allocated to random flux asymmetry.

Acknowledgments

We thank Clay Widmayer and Paul Renard for helping to set up the BTGAIN simulations. Thanks to Jerry Auerbach for providing the frequency-conversion performance code THGFT02. Thanks to Wade Williams and Ken Manes for helpful discussions regarding laser performance.

Notes and References

1. L. Powers and L. J. Suter, Lawrence Livermore National Laboratory, Livermore, CA, private communication (1991).
2. J. B. Trenholme, "Theory of Irregularity Growth on Laser Beams," *1975 Laser Annual Report*, Lawrence Livermore National Laboratory, Livermore, CA, UCRL-50021-75 (1975).
3. L. M. Frantz and J. S. Nodvik, *J. Applied Physics* **14**(8) (1963).
4. J. Auerbach, Lawrence Livermore National Laboratory, Livermore, CA, memorandum NIF-LLNL-94-516 (1994).
5. G. B. Zimmerman wrote Gertie. The user interface was written by D. H. Munro. The viewfactor subroutine was written by R. Kirkpatrick and modified by D. S. Bailey.
6. S. W. Hann et al., *Phys. Plasmas* **2**(6), 2480–2487 (1995).
7. G. B. Zimmerman and W. B. Kruer, *Comments Plasma Phys. Control. Fusion* **2**, 85 (1975).
8. J. A. Harte et al., *ICF Quarterly Report* **6**(4), 150–164, Lawrence Livermore National Laboratory, Livermore, CA, UCRL-LR-105821-96-4 (1996).
9. S. Sommer, Lawrence Livermore National Laboratory, Livermore, CA, private communication (1998).
10. S. W. Haan, Lawrence Livermore National Laboratory, Livermore, CA, private communication (1997).